



ANNUAL  
REVIEWS **Further**

Click here for quick links to Annual Reviews content online, including:

- Other articles in this volume
- Top cited articles
- Top downloaded articles
- Our comprehensive search

# Novel Detection Schemes of Nuclear Magnetic Resonance and Magnetic Resonance Imaging: Applications from Analytical Chemistry to Molecular Sensors

Elad Harel,<sup>1</sup> Leif Schröder,<sup>1</sup> and Shoujun Xu<sup>2</sup>

<sup>1</sup>Materials Sciences Division, Lawrence Berkeley National Laboratory, and Department of Chemistry, University of California, Berkeley, California 94720; email: elharel@berkeley.edu; schroeder@waugh.cchem.berkeley.edu

<sup>2</sup>Department of Chemistry, University of Houston, Houston, Texas 77204; email: sxu7@uh.edu

Annu. Rev. Anal. Chem. 2008. 1:133–163

First published online as a Review in Advance on January 15, 2008

The *Annual Review of Analytical Chemistry* is online at [anchem.annualreviews.org](http://anchem.annualreviews.org)

This article's doi:  
10.1146/annurev.anchem.1.031207.113018

Copyright © 2008 by Annual Reviews.  
All rights reserved

1936-1327/08/0719-0133\$20.00

## Key Words

microfluidics, flow imaging, low field, atomic magnetometer, molecular imaging, chemical exchange saturation transfer (CEST)

## Abstract

Nuclear magnetic resonance (NMR) is a well-established analytical technique in chemistry. The ability to precisely control the nuclear spin interactions that give rise to the NMR phenomenon has led to revolutionary advances in fields as diverse as protein structure determination and medical diagnosis. Here, we discuss methods for increasing the sensitivity of magnetic resonance experiments, moving away from the paradigm of traditional NMR by separating the encoding and detection steps of the experiment. This added flexibility allows for diverse applications ranging from lab-on-a-chip flow imaging and biological sensors to optical detection of magnetic resonance imaging at low magnetic fields. We aim to compare and discuss various approaches for a host of problems in material science, biology, and physics that differ from the high-field methods routinely used in analytical chemistry and medical imaging.

---

**NMR:** nuclear magnetic resonance

**MRI:** magnetic resonance imaging

**Remote detection:** general methodology in which encoding and detection occur in different physical or molecular environments

---

## 1. INTRODUCTION

Although nuclear magnetic resonance (NMR) is perhaps the most powerful analytical method in chemistry, its usefulness is limited in many applications by poor sensitivity. As a general rule, approximately  $10^{15}$ – $10^{18}$  spins are needed for an inductively detectable signal at high magnetic field strengths. This is mainly due to the very small nuclear magnetic moment relative to  $k_B T$  at room temperature. Consequently, NMR is performed on relatively large samples a few cubic centimeters in volume; for magnetic resonance imaging (MRI), the sample is typically several hundred cubic centimeters. Much of the work on magnetic resonance over the past 60 years has gone into combating this very problem, as the rewards for doing so are far-reaching.

High-resolution one-dimensional NMR is an everyday tool of the organic chemist (1). Multidimensional NMR allows for the structural determination of proteins in solution (2). MRI is one of the most valuable diagnostic tools available in medicine (3) and materials characterization (4).

Here, we describe a very general method, which we call remote detection, for increasing the sensitivity in NMR or MRI experiments; this method is applicable when excitation and detection can be separated in some manner. This process may involve actual physical separation of these stages of the experiment, or it may involve a chemical exchange in which information about a species in one environment is detected by examination of it in another.

First, we give a general overview of the concept. We then provide examples of the methodology's utility in various applications, including materials characterization, flow imaging, lab-on-a-chip devices, analytical chemistry, solid-state NMR, low-field MRI, optical detection of NMR and MRI, and biological sensors.

## 2. TRADITIONAL NUCLEAR MAGNETIC RESONANCE

The phenomenon of NMR is based on the interaction between an external magnetic field and the nonzero nuclear spin of certain atomic isotopes (5); this is known as the Zeeman interaction. This interaction splits otherwise degenerate energy levels and is responsible for the NMR spectrum. For molecules, the orbiting electrons of nearby atoms slightly alter the magnetic field felt by the nuclear spin. The resulting chemical shift can only be observed at very high magnetic fields and under conditions of extremely high field homogeneity. These opposing experimental conditions are responsible for the very high costs and maintenance associated with high-field NMR. Other interactions between nuclear spins that are independent of the magnetic field strength, the so-called indirect interactions, give rise to J-couplings and raise the possibility of multidimensional NMR, which would allow unambiguous assignment of peaks through a network of coupled spins. The power of NMR is in its ability to precisely control these spin interactions and to observe them by applying sequences of accurately timed radio frequency (rf) pulses and magnetic field gradients.

Such rf pulse sequences have been the focus of a tremendous amount of research since pulsed NMR was first proposed nearly 30 years ago (6). In pulsed NMR, the spins are encoded into the desired quantum mechanical state. Detection is accomplished by the reverse process, whereas a changing magnetization resulting from the ensemble

spin state is converted into a small but detectable electronic signal. Typically, encoding and detection are performed with a single rf coil, which surrounds the sample of interest. The coil may be ideal for encoding but will suffer drastically for detection if the region of interest is small in comparison to the coil (7). This is often the case for heterogeneous samples, including organs of the body, porous materials, and microfluidic devices. This restriction may also apply in the case of a very dilute chemical species surrounded by a large solvent bath, in which the former is difficult to detect.

### 3. REMOTE DETECTION BASICS

The first modality of remote detection that we discuss challenges this paradigm by physically separating the encoding and detection steps of an NMR pulse sequence so as to optimize each step individually. In remote detection NMR, a large rf coil encompasses the sample while a smaller coil concentrates the signal for more efficient and sensitive detection (8, 9). This separation allows for the possibility of moving away from inductive detection altogether and implementing optical detection and other noninductive schemes (discussed below). Regardless of the detection modality, the principle of separate encoding and decoding remains the same.

**Figure 1** illustrates a generic remote detection scheme. At equilibrium the nuclear spins align in the direction of the static field. A selective pulse excites the spins according to their location in space or chemical shift or both. As in any other NMR or MRI pulse sequence, the spins experience either free evolution or evolution according to a well-defined sequence of rf and gradient pulses, which places the magnetization into a certain desired state. In traditional magnetic resonance experiments, readout is performed at this junction. In remote detection, the phase of the spins in the transverse plane must be stored along the longitudinal direction so as to be affected only by spin-lattice relaxation,  $T_1$ . Because  $T_1$  is typically much longer than  $T_2^*$ , the effective transverse relaxation time, the spins can effectively flow out to the detector before an irreversible loss in signal occurs. At the detection stage, readout of the stored magnetization provides information about the phase, which in turn provides a complete description of the desired spin state (as in traditional NMR). Because the detector typically has a smaller volume than the encoding volume, several pulses are needed to completely detect the encoded magnetization. This results in a travel curve, which measures the time of flight (TOF) of encoded spins to the detector.

Because the first spins to arrive are typically unencoded, the signal is at a maximum value. As encoded spins arrive they mix with unencoded spins, causing a decrease in the overall signal that can be observed by a dip in the TOF curve. As the encoded spins leave the detector, the signal is restored. The conventional time dimension is no longer available as the direct dimension because the encoding coil is used only to manipulate the magnetization, so encoding must proceed point by point. For example, a free induction decay (FID) is usually measured by exciting the spins into the transverse plane and then acquiring the signal over time. In remote, points along the FID are recorded by delaying the time between the storage and detection pulses. Each point in the travel curve thus contributes one point to the indirect interferogram

---

**Effective transverse relaxation:** spin dephasing in the transverse plane due to the combined effects of spin-spin interactions and magnetic field inhomogeneities

**Time of flight (TOF):** time needed for an encoded spin to reach the detection region

**FID:** free induction decay

---

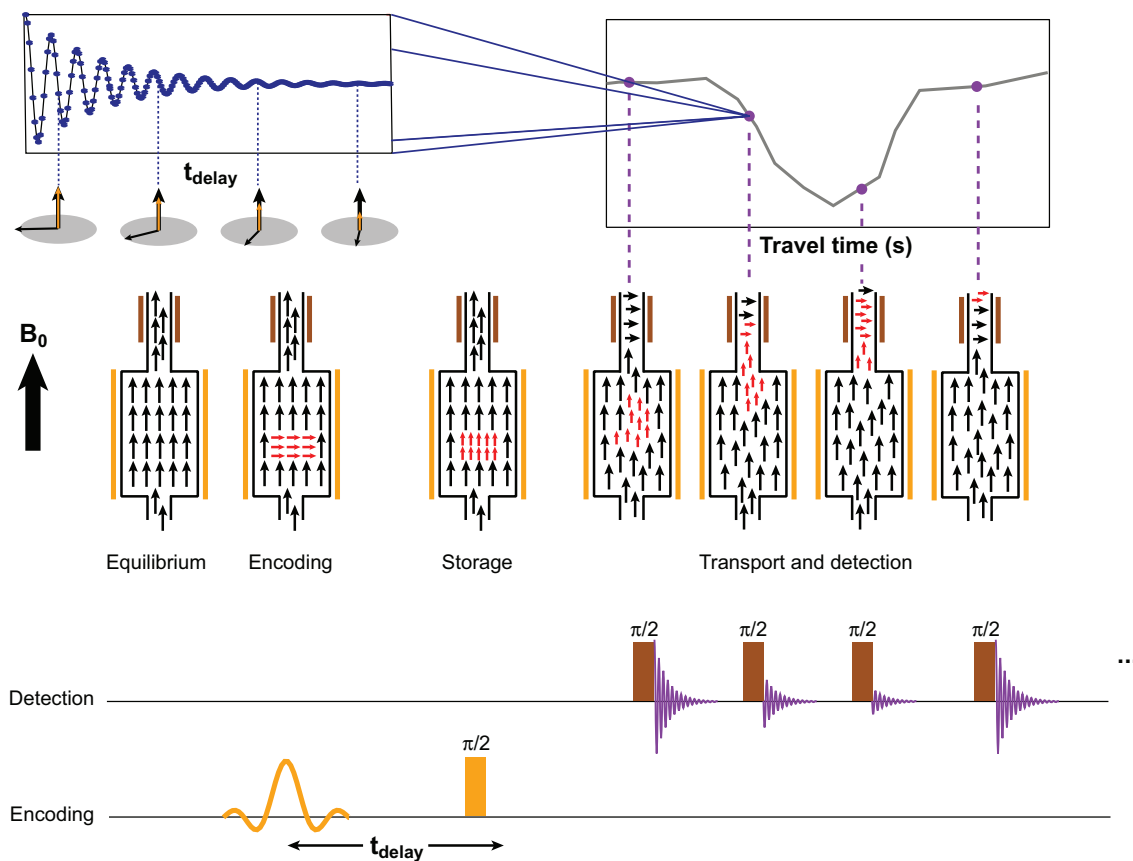


**Figure 1**

General remote detection scheme. A selective pulse excites the spins of interest. The magnetization precesses about the static field, acquiring phase which gives either spectroscopic (free evolution) or imaging (evolution in the presence of gradients) information about the sample. A storage pulse converts the phase information into longitudinal magnetization, which is subject only to  $T_1$  relaxation. The spins then flow to the detector, which reads out the amplitudes by a train of hard pulses. Each detection pulse contributes one point to the time-of-flight (TOF) curve. Repeating the experiment point by point creates an interferogram (*upper left*) that decays, i.e. the free induction decay (FID). In the case of spectroscopy, this corresponds to incrementing the delay between the encoding and storage pulses, creating an indirect FID. In the case of imaging, the delay is fixed and the gradient strength is incremented which covers  $k$ -space (the reciprocal space in which the signal is acquired prior to Fourier transformation). Each detection pulse then creates a partial image corresponding to the spin density in the sample, which arrives at the same TOF to the detector. The sum of these partial images creates the full image of the sample.

(e.g., FID) built up by repeating the remote experiment, each time with a different indirect point (e.g., time delay). In the following sections we illustrate these ideas more concretely with several examples.

### 3.1. Gas Flow Imaging in Porous Materials

**Figure 2a,b** illustrates the results of a remote experiment using hyperpolarized xenon gas flowing through a porous rock (10). Optical pumping methods allow thermally polarized xenon to be enhanced from a thermal polarization of about  $10^{-5}$  to 2–5% (11, 12), which corresponds to an increase in sensitivity of over three orders of magnitude. The increased sensitivity allows gas mixtures containing xenon to be visualized with MRI even though the density of the gas is much lower than that of a liquid. For applications related to crude oil recovery, pore-level structural determination, and materials characterization, gas flow imaging is critical (13). The images in **Figure 2** were obtained using a simple phase-encoding scheme applied to xenon gas flowing through a Bentheimer sandstone rock with a porosity of about 22.5% and pore size of approximately 100  $\mu\text{m}$ .

The entire data set consists of the spatial dimensions and the additional TOF dimension. Projecting along the TOF dimension provides the full three-dimensional image as shown in **Figure 2b**. Cutting a wedge out of the data set reveals flow inhomogeneities, such as regions of spins that rapidly dephase either because of incoherent flow or  $T_2^*$  relaxation or because of static spins that never reach the detector within the  $T_1$  relaxation time of the gas. A direct image would show such inhomogeneities in the former case, but not the latter. Thus, by comparison with direct imaging, insights into the flow can be elucidated.

Notably, the partial images corresponding to different points along the TOF dimension are not real-time images of the flow as in fast, direct imaging sequences such as echo planar imaging (EPI) (14). Rather, they are a spatial representation of spins that take an equal amount of time to reach the detection region. Remote detection, therefore, is much more similar to chromatography used in chemical analysis. As a result, the first images represent spins that typically initiate from the outlet region and that take the least amount of time to reach the detection region. Later TOF values correspond to spins that take longer to reach the detector. Therefore, the geometry of the sample plays an important role in determining the spatial profiles of each partial image, as it determines to a large degree the necessary flow path for a given packet of encoded spins.

In this example, investigators utilized hyperpolarized xenon to trace gas flow through a porous material. However, xenon has another remarkable property in addition to its ability to become highly polarized: It displays a wide range of chemical shifts that are very sensitive to the chemical or physical environment (15). Proton NMR exhibits a chemical shift range of about 8 ppm. Xenon, on the other hand, can exhibit a range of more than 7000 ppm arising from its highly polarizable electron cloud. In nanoporous materials such as silica aerogel, xenon shows a chemical shift range of up to  $\sim 120$  ppm depending on the size of the pore within which it is enclosed (16). In the large macropores of the aerogel, the xenon chemical shift approximates

---

**Hyperpolarization:**

polarization of spin states that significantly exceeds the state populations given by the Boltzmann distribution

**EPI:** echo planar imaging

---

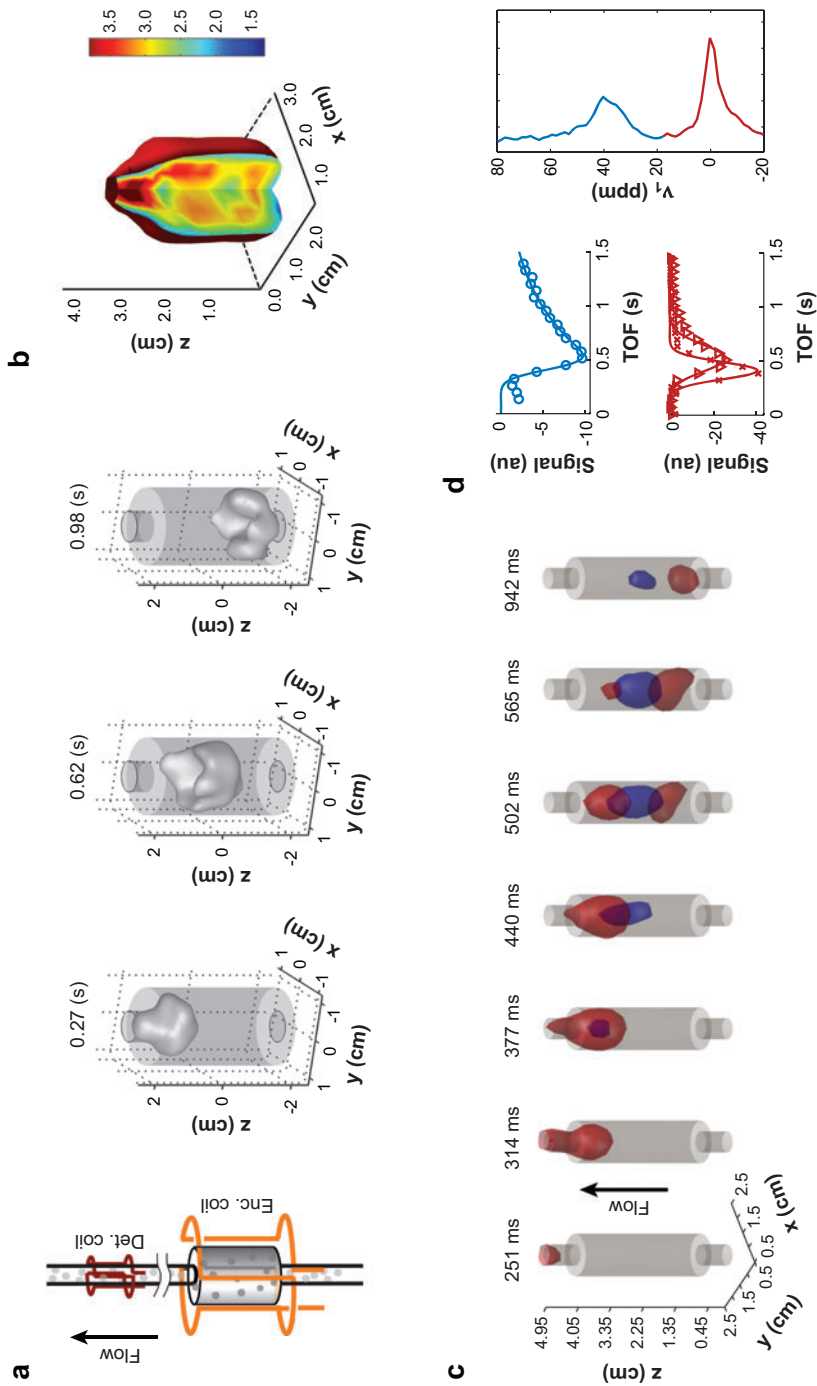


**Figure 2**

Xenon flow through a porous Bentheimer rock. (a) Images acquired by applying a hard pulse and then incrementing the gradient strength prior to the storage pulse, resulting in the creation of a full three-dimensional image. The first partial image corresponds to the spin density that took 0.27 s to reach the detector. Similarly, the last partial image corresponds to spins that took 0.98 s to reach the detector. (b) Full image, reconstructed by projecting the data along the time-of-flight (TOF) dimension. Regions of low intensity arise either from low spin density, fast  $T_2^*$  relaxation, stagnant flow in which spins never reach the detector within  $T_1$ , or incoherent flow (e.g., turbulence). (c) Three-dimensional isosurfaces of xenon flow through aerogel. Spin density from free xenon gas (red) and occluded gas (blue) are represented. (d) TOF curves for regions inside the aerogel (blue circles) and inlet (red triangles) and outlet (red squares). Dispersion causes a broadening of the Gaussian profiles from outlet to inlet as the latter must travel a longer distance to the detector. The width of the aerogel TOF curve is broader than that of the inlet although the distance to the detector is shorter, indicating the presence of two distinct flow paths. The long exponential tail is the result of dead-end pores that are poorly connected to the main flow field, which provides a path to the detector.

that of the free gas, which is 0 ppm. In the mesoporous region, at about 20–30 nm, the xenon chemical shift measures  $\sim 38$  ppm at room temperature (17). The correlation between chemical shift and pore size allows MRI to indirectly probe the nanoporous environment of the aerogel even when the actual MRI spatial resolution is several orders of magnitude lower than that needed to resolve the pore structure directly.

Radio frequency pulses can easily tag one spin species over another at large frequency separations by employing short bandwidth pulses. **Figure 2c,d** illustrates the results of two experiments of xenon gas flow through aerogel, each selecting a different resonance peak (18). The flow of the free gas (0 ppm) can thus be distinguished from the flow of the occluded gas (38 ppm).

Dispersion can be described in either the spatial domain or the time domain (19). In the former, the spreading of a fluid in a given time interval is measured, whereas in the latter, the arrival time distribution of a tagged fluid is examined. In remote detection, this time distribution is represented by the TOF curve, the width of which is a measure of dispersion. If we assume that the flow in an unrestricted geometry is described by a normal distribution, then we can assign a width and mean time for each voxel in the image. The fit of a normal distribution to the TOF curve is fairly good, validating this approximation. Mathematically, we have

$$s(t, \mathbf{r}) = s_0(\mathbf{r}) \Delta t \exp(-(t - t_0(\mathbf{r}))^2 / 2\sigma(\mathbf{r})^2) / \sqrt{2\pi}\sigma(\mathbf{r}). \quad (1)$$

Therefore,  $\sigma(\mathbf{r})$  and  $t_0(\mathbf{r})$  can be assigned to each position  $\mathbf{r}$ . For voxels inside the aerogel itself, however, this model no longer applies. Instead, we find that a Gaussian convoluted with an exponential decay accurately models the TOF curves. Once again, we can assign  $\sigma(\mathbf{r})$  and  $t_0(\mathbf{r})$  to each position  $\mathbf{r}$ . Additionally, we can assign a time constant  $\tau(\mathbf{r})$  to yield a measure of how well the occluded gas is connected to the main flow field, which provides a coherent path to the detection region. Therefore, by selecting each peak separately we are able to identify two completely separate flow paths and image each individually with a high time resolution (**Figure 2c**). The physical explanation for this observation is that the xenon inside the small mesopores of the aerogel is not well connected to the main flow field, most likely due to the presence of dead-end pores inside the sample.

Unlike other methods that identify porosity (20), pore-size distribution (21, 22), and other bulk values, remote detection flow imaging provides material heterogeneities. That is, material properties can be measured for each voxel in the image. It should be noted that, even in principle, optical techniques could never perform such an experiment because the occluded and free gas have identical physical properties. Furthermore, many samples of interest are opaque and thus inaccessible to optical wavelengths. Numerous porous materials show a large chemical shift range for xenon (23) and are amenable to these methods.

### 3.2. Lab-on-a-Chip: Imaging and Spectroscopy

As a noninvasive spectroscopic technique, NMR presents an attractive complementary approach to optics-based detection methods for lab-on-a-chip devices (24). Microfluidics shows great promise in the fields of biology, chemistry, and physics

due to its unique ability to precisely control fluids at very small volumes (25). Its applications range from DNA analysis (26), proteomics (27), and synthetic chemistry (28) to fundamental studies of physical processes (29). Optics-based detection methods generally suffer from a lack of chemical specificity and limit the use of microfluidic devices to only those made from optically transparent materials (30). Although some spectroscopic techniques (such as Raman and IR) have been applied to microfluidic devices (31), they are inhibited to a large extent by the very short optical path length through the microchannels of the devices (32). Furthermore, they are generally limited to examining only a single point on the chip at a time. NMR also suffers from a significant loss in sensitivity due to the very small volume of analyte on the chip and the necessarily large coil (which is several orders of magnitude larger than the individual channels) surrounding the entire microfluidic device. Remote detection allows this sensitivity limitation to be overcome and has proved ideal for the analysis of microfluidic devices. For microfluidic chips it offers the ability of full-chip imaging, spectroscopy, and flow analysis—all at very high sensitivity.

The experiment described below (also see **Figure 3**) involves the mixing of two fluids inside a simple mixing microfluidic chip. In one channel flows ethanol, in the

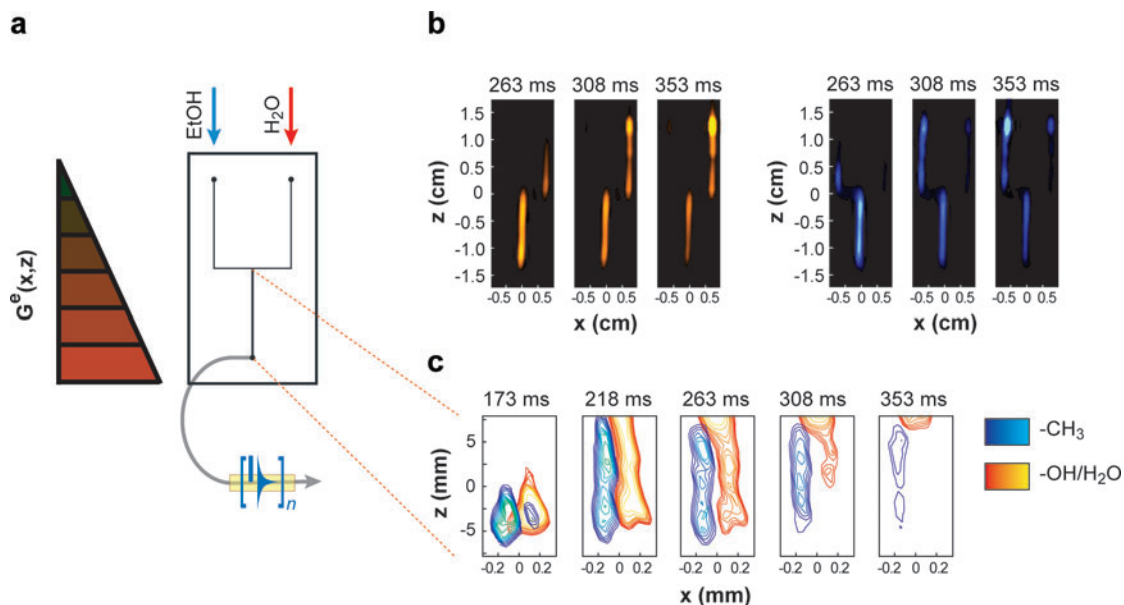


**Figure 3**

Liquid flow imaging through a complex microfluidic chip. (a) Ethanol (blue arrow) and water (red arrow) flow through a T-mixer chip. The detection volume is less than 50 nL. Also shown is the symbol for the magnetic field gradient necessary for imaging (red triangle). (b) Spectra. Even though the spectra are not resolvable inside the chip, they are highly resolved outside the chip. The flow of each species can be distinguished and subsequently imaged by selecting the appropriate resonance peak in the detector. (c) A zoomed-in view of the mixing region shows that the fluids in fact do not mix at this flow rate.

other flows water. As mentioned above, the chemical shift range of protons is rather small, thus magnetic field homogeneity is critical. Unfortunately, the interface between the glass and fluid causes severe local magnetic field gradients because of the difference in magnetic susceptibility between the different materials and their geometry (33). This effectively makes resolving the chemical shifts of the different species impossible directly on the chip. Although there may be methods of overcoming this limitation, such as using susceptibility-matched materials, they are not applicable to existing microfluidic chip designs.

Remote detection can circumvent this inhomogeneity problem. Once the fluids exit the chip and pass through the small solenoid detection coil, the spectrum is highly resolvable (34). For this particular chip, the resolution decreases from 5 kHz to less than 50 Hz upon exiting the chip—an improvement of two orders of magnitude. This allows the flow of each species to be resolved even when the chemical shift is not directly resolvable. In this way, any number of species can be resolved and imaged in a single experiment as long as the residence time in the detection coil is long enough to resolve the peaks.

Furthermore, unlike other methods that perform NMR on a chip, remote detection is capable of imaging the entire chip or a section thereof with very high sensitivity. Direct NMR-on-a-chip methods fabricate the detection coil directly onto the chip, greatly enhancing sensitivity (35). However, this means that only a few coils can be placed on the chip at once as their fingerprint is rather large ( $> 1$  mm in diameter); furthermore, the chip fabrication must be significantly altered. Again, magnetic susceptibility becomes a major problem as the addition of a new element, the copper surface coil, creates severe magnetic field distortions. Additionally, this method is not compatible with most of the chip fabrication techniques already in place. Nonetheless, NMR on a chip, whether remote or direct, promises to become a growing area of research.

### 3.3. Solid-State Nuclear Magnetic Resonance

So far we have discussed enhancing the detection sensitivity of liquid samples. It is also possible to employ a type of remote detection for very high sensitivity detection of solid samples. Due to the dipolar interaction between spins, which are averaged away in isotropic samples, NMR spectra of solids are very broad unless spun at the “magic” angle,  $\theta \sim 54.7^\circ$ . This is because of the dominant term in the dipolar Hamiltonian, which has the form  $(3 \cos^2 \theta - 1)$ , where  $\theta$  is the angle between the internuclear vector and the external field. Magic angle spinning, which averages away these broadening terms, does have a drawback: The spinning rotor needed to hold the sample is large compared to mass-limited samples. The solution to this problem has been demonstrated in an experiment by Sakellariou et al. (36) in which two coils were used, a static coil for sample spin manipulation and detection that was inductively coupled to a very sensitive microcoil wrapped directly around a glass capillary containing the sample. Susceptibility problems were eliminated due to the presence of coil material and sample interface in liquid microcoil designs (37). This method has important applications to the analysis of biological tissue, organic powders, and radioactive material.

### 3.4. Perspectives and In Vivo Applications

Remote detection, which was initially utilized solely to enhance sensitivity, is a very powerful method for elucidating the fluid flow properties of porous materials. Adding spectroscopy in the encoding and detection regions allows the applicability of this method to a large class of systems, from porous rocks and nanoporous materials to microfluidics. In vivo applications, where spins are excited in the brain and detected in the jugular where the blood collects, may also be possible (38). Such applications would allow much higher sensitivity imaging in regions of the brain far below the surface of the skull where the head coil is most insensitive. Furthermore, such a modality would allow for optical detection of the NMR signal and, possibly, low-field encoding (see **Figure 4** for an illustration of this potential medical application). Because flow is ubiquitous in nature, NMR remote detection may also be applicable to many other systems of biological significance, including diffusion across biological membranes and the study of protein/ligand binding events.

In the following section, we provide an overview of another remote detection method in which chemical exchange replaces the physical transport of a fluid, as in the applications described earlier. This method has very important implications for molecular and biological sensors.

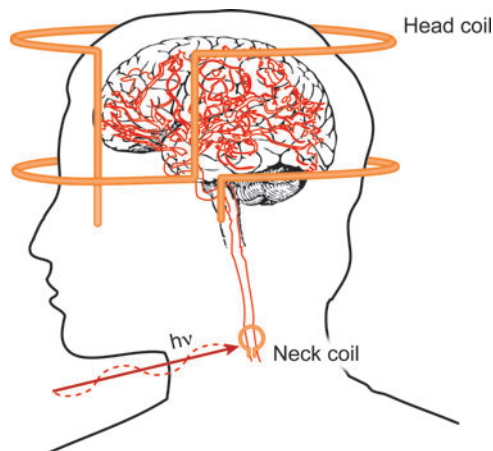


**Figure 4**

Potential in vivo applications of remote detection. Although magnetic resonance imaging (MRI) offers very high resolution images of the brain, it suffers from a severe lack of sensitivity of regions buried deep inside the brain. Such regions, however, are critically important in stroke and other diseases. Coil sensitivity falls steeply with the distance of the coil to the region of interest. Blood flow in the brain, however, transfers blood from most regions of the brain and collects at the jugular vein near the surface of the neck where a sensitive neck coil could potentially be positioned for an increase in sensitivity. This may provide a modality for very high resolution imaging in regions not currently accessible by current MRI methods. Detection could also proceed by optical detection which would measure the magnetic flux of the encoded blood.

## 4. INDIRECT NUCLEAR MAGNETIC RESONANCE DETECTION BASED ON CHEMICAL EXCHANGE

Biomedical NMR applications require enhanced sensitivity for diagnostic purposes in the rapidly expanding field of molecular imaging. In this context, a special version of remote detection comes into play. The inherently low sensitivity of NMR limits the detection of molecules (other than water) for imaging in order to reveal biochemical abnormalities at very early stages of diseases. Hence, proton MRI currently is not the first choice for molecular imaging (39). To expand the capabilities of biomedical NMR, the problem of sensitivity can be tackled by indirect detection methods that rely on chemical exchange of selectively saturated magnetization. This is, in principle, an in situ version of remote detection that separates the molecular environment of the detection from the encoded molecular information. There are two ways to implement this approach in order to significantly amplify the signal from a low-concentration target molecule: either via exchange with a huge reservoir of thermally polarized spins, or by using a reservoir of only medium size that is, however, hyperpolarized.

Historically, the thermal polarization method was first realized by using chemical exchange saturation transfer (CEST) (40) to detect exchangeable protons of the OH, NH<sub>2</sub>, and NH groups of several sugars, amino acids, nucleosides, and other compounds after selective saturation (i.e., depletion of the magnetization) at 1–6.5 ppm downfield of the water resonance and subsequently observing changes in the abundant water signal. An expansion of the concept involving xenon gas that was hyperpolarized through laser polarization was presented recently (41) and differs from the former method in various aspects (discussed below).

Both concepts have the following principle in common: The chemical exchange in combination with adjustable, selective rf pulses allows detection of information from the molecular species at low concentration by encoding it in a way that enables remote amplification, resulting in a high-intensity signal (**Figure 5a**). Whereas conventional detection acts like a snapshot technique, reading only signal from the few nuclei that are actually bound to the target molecule, the CEST approach involves many hundreds to thousands of participating nuclei per second at each exchange site in the labeling process and thus “stores” the preamplified information.

### 4.1. Theory of the Chemical Exchange Saturation Transfer Enhancement Method

The basic idea of the CEST technique was first demonstrated in a double resonance experiment by Forsén & Hoffman (42) in a study of the chemical exchange between two compounds of similar concentration. The authors analyzed their data based on differential equations describing the dynamics of a two-site exchange system as proposed by McConnell in terms of modified Bloch equations (43). The detection pool is denoted by index *d* and parameters of the saturated pool are indexed *s*; the observed longitudinal magnetization,  $M_z^d$ , decreases upon irradiation on the frequency of  $M_z^s$ . The parameters to quantify the chemical exchange are the lifetimes  $\tau^d$  and  $\tau^s$  of the exchangeable nuclei in the two environments. Under the assumption of achieving

---

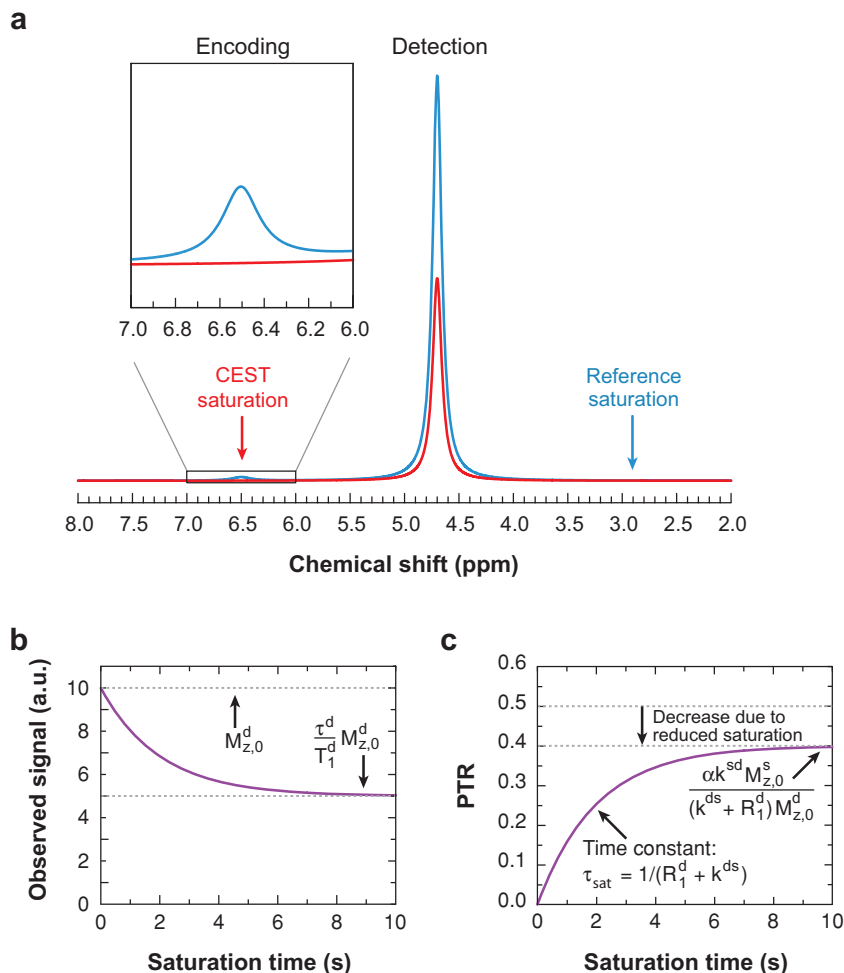
**Molecular imaging:** illustrates the spatial distribution of specific molecules of biochemical relevance

**CEST:** chemical exchange saturation transfer

---

**Figure 5**

(a) Schematics of the chemical exchange saturation transfer (CEST) method using molecular separation of encoding and detection for significant signal amplification. The resonance of the detection molecule at high concentration (in this case, water) is observed after off-resonance saturation (*blue spectrum*) and after on-resonance saturation (*red spectrum*) of a highly diluted CEST agent. (b) Decrease in the observed signal assigned to  $M_0^d$ , assuming complete saturation of  $M_z^s$ . The time constant  $\tau_{\text{sat}}$  and the amplitude of the new steady-state magnetization are determined by the longitudinal relaxation rate  $R_1^d = 1/T_1^d$  and the exchange rate from the detection pool into the saturation pool,  $k^{ds} = 1/\tau^d$ . (c) Proton transfer ratio (PTR) from the data in (b) assuming an incomplete saturation with  $\alpha = 0.8$ .



$M_z^s = 0$  instantaneously, the new equilibrium of  $M_z^d$  is reached in a monoexponential decay (Figure 5b).

An important precondition for CEST is that the saturation field be selective enough to neglect direct saturation of  $M_z^d$ . The first papers on CEST illustrated the so-called spillover effect of the detected water resonance at 4.7 ppm in so-called z-spectra (42, 44), which allow a comparison of the desired saturation effect at 4.7 ppm +  $\delta$  with a control signal after saturation at 4.7 ppm -  $\delta$ . Although proton CEST experiments deal with chemical shift differences of at least 300 Hz, pulsed rf signals have a non-negligible minimum bandwidth. Therefore, their amplitude is adjusted to minimize spillover effects. Realistic conditions are given by the weak saturation pulse approximation that allows for incomplete (but still instantaneous) saturation of  $M_z^s$ . For this purpose, the concept of the proton transfer ratio (PTR) (45)

**Spillover effect:** unwanted direct saturation of a spin ensemble while saturating another spin ensemble at different resonance frequency

**PTR:** proton transfer ratio

was introduced, which includes the saturation efficiency  $\alpha$  of the saturated resonance to modify the above-mentioned signal change (**Figure 5c**). Theoretical analysis of the underlying dynamics of CEST agents (45) yields:

$$\text{PTR} \equiv \frac{M_{z,0}^d - M_z^d(t)}{M_{z,0}^d} = \frac{\alpha k^{sd} M_{z,0}^s}{(k^{ds} + R_1^d) M_{z,0}^d} \left(1 - e^{-(k^{ds} + R_1^d)t}\right). \quad (2)$$

The time constant for the exponential behavior of both parameters is still  $1/\tau_{\text{sat}}$ . The magnetizations  $M_z^d(t)$  and  $M_{z,0}^d$  are determined from the signal intensities with on- and off-resonant saturation and subsequent correction of so-called magnetic transfer (MT) effects that possibly overlap with the CEST effect (46, 47) (see **Figure 6a**). Equation 2 shows that the PTR is directly proportional to the concentration of the

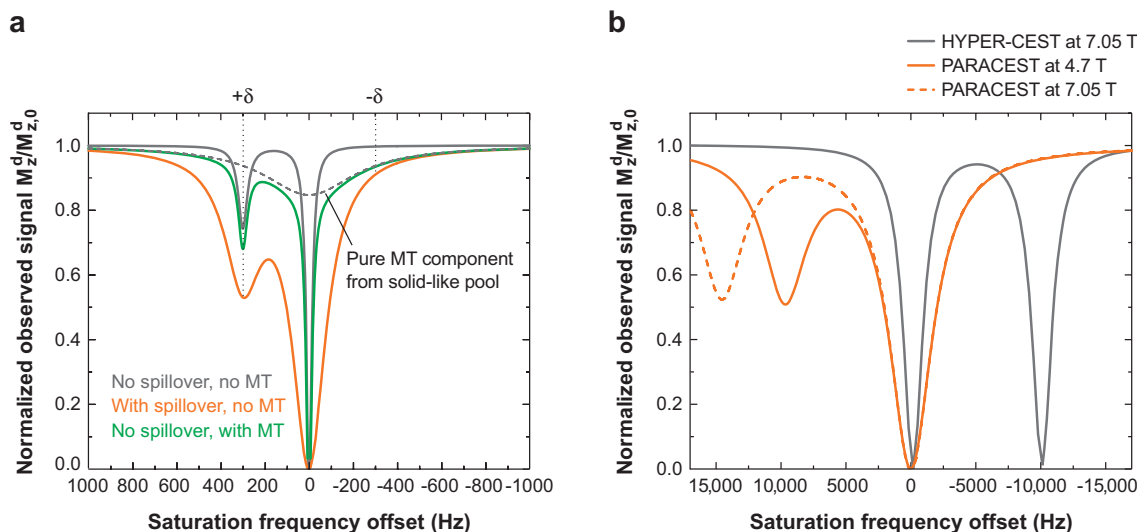


**Figure 6**

(a) Schematic representation of z-spectra for different scenarios of chemical exchange saturation transfer (CEST) with thermally polarized protons and no chemical shift reagents. Low saturation powers (*black curve*) yield profiles with one sharp peak at the resonance of the CEST agent ( $+\delta$ ) and one peak for direct water saturation with no spillover effect observed at  $-\delta$ . Higher saturation powers (*red curve*) increase the saturation bandwidths and lead to unwanted saturation at  $-\delta$ . Magnetic transfer (MT) effects can yield an additional signal decrease that must be separated from the CEST effect. Such MT effects are only relevant in the presence of a solid-like spin ensemble, such as immobilized water in vivo (*dashed resonance profile*), which causes an extremely broad dip in z-spectra. For further details, see References 46 and 47. (b) z-spectra comparing a paramagnetic CEST (PARACEST) agent at 4.7 T (schematic representation according to results in Reference 55) with hyperpolarized xenon CEST (HYPER-CEST) of a functionalized xenon biosensor at 7.05 T. Both show frequency separations from the detection signal on the order of 10 kHz, but PARACEST is related to fast exchange, thus showing broad dips in the saturation profiles. The spillover effect, around  $-10$  kHz, is negligible for both agents. Simulation of the PARACEST spectrum for 7.05 T shows a better separation of the two saturation dips. However, the HYPER-CEST profile is still sharper.

---

**APT:** amide proton transfer

---

saturated pool.  $\alpha$  is defined via the power  $\omega_1 = \gamma B_1$  of the saturation pulse in Hz and two parameters  $p$  and  $q$  that take transverse and longitudinal relaxation effects into account (for details, see Reference 48):

$$\alpha = \frac{\omega_1^2}{\omega_1^2 + pq}. \quad (3)$$

Hence, powers must be adjusted to minimize the relevance of  $pq$  and to achieve  $\alpha \rightarrow 1$  (full saturation). One important contribution to incomplete saturation is exchange-line broadening that reduces  $T_2$  and increases  $p$ .

## 4.2. Diamagnetic Chemical Exchange Saturation Transfer Agents and Applications

CEST experiments using thermally polarized protons can be divided into two groups: diamagnetic CEST (DIACEST) and paramagnetic CEST (PARACEST). The first group represents the “classic” CEST agents that contain no paramagnetic shift reagent. Several kinds of biochemical compounds were studied and yielded different signal enhancements due to various exchange characteristics. As seen in Equation 3, a high exchange rate  $k^{ds}$  and a slow (long)  $T_1$  relaxation are favorable to achieving a high PTR. Hence, such experiments are predestined for high magnetic fields to assure both small  $R_1^d = 1/T_1^d$  and large chemical shift separation. The first CEST candidates investigated by Ward and colleagues were studied at concentrations between 62.5 mM and 250 mM to achieve saturations between 10–67% of the 111-M water proton signal (40). The enhancement of, for instance, barbituric acid under physiological conditions (pH = 7.4,  $T = 37^\circ\text{C}$ ) was quantified as 264-fold and used for demonstration of pH-sensitive imaging. Because the contrast depends on both concentration and the pH-adjustable exchange rate, Balaban and colleagues later introduced a method using agents with more than one type of exchangeable proton to calibrate for pure pH-dependence while eliminating concentration effects (49).

The second generation of DIACEST agents included compounds with high numbers of exchangeable protons. Cationic polymers at concentrations of  $\sim 10^{-4}$  M were reported to cause water signal changes of 40–50% (50). Poly-L-lysine (PLL), for example, involves more than 7000 exchangeable sites, thus yielding an enhancement factor of more than 486,000. Polyuridilic acid, a polymer of 2000 uridine units, was observed at 10  $\mu\text{M}$  with an enhancement factor of  $\sim 10.8 \times 10^6$  via its imino protons (51).

The amide protons of some endogenous compounds were used in a method called amide proton transfer (APT) to detect pH changes via the exchange rate shown in Equation 3. This approach is of special biomedical interest because the rates reflect tissue pH and local biochemical parameters such as salt or metal content. It was used to study ischemic brain related to acute stroke (46) and to reveal brain tumors in mice (52). Two CEST-related methods have been proposed (53) to determine the base catalyzed, the acid catalyzed, and the spontaneous exchange rate constants for very low concentrations of amide protons in polyamide-based APT agents. In such applications, conventional methods such as the quantification of exchange line

broadening would be very time consuming because of the low signal-to-noise ratio related to direct observation of such dilute protons.

### 4.3. Limitations of Conventional $^1\text{H}$ Chemical Exchange Saturation Transfer Detection

One limiting factor of DIACEST compounds is the small chemical shift range of protons. This has two consequences: (*a*) the slow exchange condition needed for resolving signals of two sites in exchange is relatively strict, thus limiting the maximum observable rate; and (*b*) the spillover effect due to direct saturation of the relatively close detection signal requires a trade-off between saturation power and unwanted signal reduction. Agents with a larger chemical shift separation would therefore significantly improve the capabilities of the CEST enhancement and could be detected at lower concentrations.

Spillover effects are of minor importance as long as the amplitude of the saturation pulse (given in Hz) is negligible compared to the chemical shift difference (in Hz) between the saturated and the observed resonance (54). At 4.7 T, the frequency separation of the saturated protons of PLL from the detected water signal is approximately +700 Hz and a saturation pulse amplitude of 0.5  $\mu\text{T}$  (corresponding to  $\sim 21$  Hz) causes no spillover. In contrast, a 3- $\mu\text{T}$  pulse ( $\sim 128$  Hz) yields a CEST decrease of  $\sim 30\%$ , but the off-resonance saturation at  $-700$  Hz is also related to a signal change of  $-25\%$ . Performing such studies at 11.7 T is one loophole (albeit an expensive one) exploited to increase the chemical shift difference to approximately 1.8 kHz. Then, saturation pulses up to 250 Hz (i.e.,  $\sim 6$   $\mu\text{T}$ ) can be used, as the spillover-based signal decrease is only 3% (53).

### 4.4. Improvement through Paramagnetic Chemical Exchange Saturation Transfer

Incorporation of paramagnetic shift reagents close to the exchangeable protons improves proton CEST agents by increasing the frequency difference between water and the saturated pool. Introduced by Zhang et al. (55), the first agent was based on saturation of the bound water signal of a  $\text{Eu}^{3+}$  complex formed by a DOTA-tetra(amide) derivative. With a chemical shift separation of 49.7 ppm (9.8 kHz at 4.7 T) relative to free water, a saturation of 61% was achieved, whereas the reference experiment with saturation at  $-9.8$  kHz showed no spillover effect. Some PARACEST agents are now used with saturation powers up to 250  $\mu\text{T}$  ( $\sim 10.6$  kHz) at 7 T (56).

Reviews by Sherry et al. (57, 58) summarize the factors that allow for constructing such agents by slowing down the usually very fast exchange of water at the inner-sphere coordination sites of lanthanide(III) derivatives of DOTA. However, the short lifetimes of the bound water cause broad saturation dips in the  $z$ -spectra (see **Figure 6b**) and decrease the selectivity of the PARACEST agents. A comparison of different complexes showed that only those with  $\text{Eu}^{3+}$ ,  $\text{Tb}^{3+}$ ,  $\text{Dy}^{3+}$ , and  $\text{Ho}^{3+}$  have the right combination of water-exchange time and induced chemical shift to be potential candidates for  $B_0 < \sim 10$  T (57). Nevertheless, these agents hold great

---

**Xenon biosensor:** a molecular construct using encapsulated xenon and a targeting unit to sense biochemical targets

---

potential in terms of detection threshold, as agents with highly shifted bound water ( $\sim 500$  ppm) can be detected at concentrations of only  $10 \mu\text{M}$ .

Exchangeable protons of NH groups in addition to the coordinated water molecules in the same complex also turn PARACEST agents into sensitive pH probes (59, 60). Moreover, the use of different lanthanides makes PARACEST agents potential candidates for multiplexing (i.e., detecting different targets in the same setup). By using the different saturation resonances of bound water in an  $\text{Eu}^{3+}$  (+50 ppm induced shift) and a  $\text{Tb}^{3+}$  ( $-600$  ppm induced shift) dotamGly complex, Aime and colleagues demonstrated selective in vitro cell imaging of two marked cell populations incubated with either of the PARACEST probes (40 mM concentration) (56).

#### 4.5. Combining Chemical Exchange Saturation Transfer with Hyperpolarized Nuclei

Exchangeable hyperpolarized nuclei also allow for transferring NMR information from a molecule into a different environment in terms of in situ remote detection (61, 62). Hence, the concept of combining the CEST amplification scheme with the advantages of hyperpolarized nuclei such as  $^{129}\text{Xe}$  can resolve some of the remaining limitations of PARACEST. As has been demonstrated (41), this combination significantly increases the capabilities of NMR for sensing biochemical targets, especially for molecular imaging (**Figure 7a,b**). The main improvements compared to thermally polarized nuclei are as follows:

1. Signals of xenon associated with other molecules show an intrinsically huge chemical shift range compared to free dissolved xenon in solution (63). Hence, no paramagnetic agents are required to reduce spillover effects to negligible, even if experiments would be performed at field strengths of  $\sim 1$  T. Unlike the protons of PARACEST agents, however, the exchange rates of atomic xenon are relatively slow and yield more selective saturation dips in z-spectra (**Figure 6b**) and can be used for multiplexing with different sensors at the same time (64).
2. At the same time, the slow exchange causes no problems in terms of transfer efficiency because  $T_1$  relaxation for hyperpolarized xenon in solution is extremely slow compared to the saturation time. Therefore, the depolarization is stored much more effectively in the bulk pool than in the case of thermally polarized protons that underlie competing relaxation effects. Complete saturation can be easily achieved, and CEST with hyperpolarized xenon (HYPER-CEST) benefits from the full dynamic range of the bulk signal.

Implementation of HYPER-CEST was made possible by using molecular cages such as cryptophanes (65) as hosts to trap the noble gas for some milliseconds and make it sensitive to selective saturation. To obtain biochemical specificity, such cages can be incorporated in so-called xenon biosensors (66), in which the cages are linked to targeting units for reporting a specific binding event (**Figure 7c**). This modular setup allows, in principle, functionalization of the CEST-active site for any target that can bind a ligand or antibody. The prototype was a biotinylated cage constructed for sensing avidin. Increasing temperature is known to accelerate chemical exchange

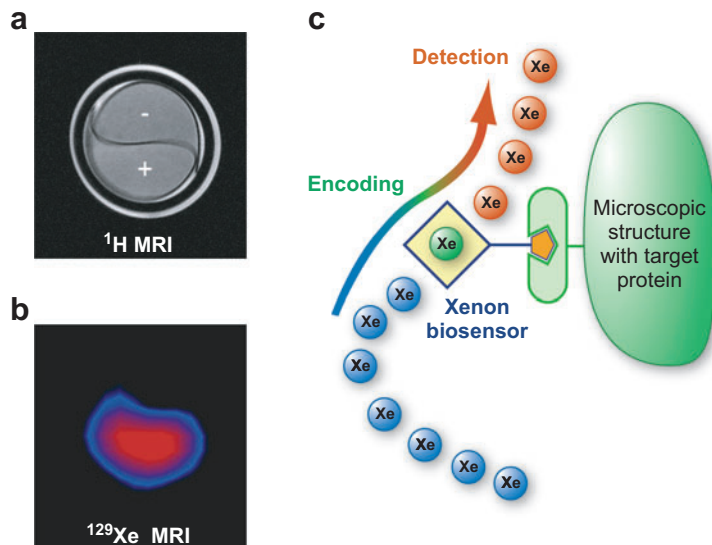


**Figure 7**

(a) Proton magnetic resonance image (MRI) showing a two-compartment phantom with avidin-labeled agarose beads. The lower compartment also contains a xenon biosensor that targets the protein. (b)  $^{129}\text{Xe}$  MRI obtained after subtracting the hyperpolarized xenon chemical exchange saturation transfer (HYPER-CEST) data set with on-resonant sensor signal saturation from control data with off-resonant saturation. Only the area containing the sensor shows the CEST contrast; other areas remain dark in the difference image.

(c) Functionalized biosensors act as host for exchangeable xenon that can be labeled using the CEST method for in situ remote detection of biochemical binding events. Data in (b) is from a biotinylated sensor that interacts with the protein avidin, which is attached to the surface of microscopic agarose beads.

significantly for  $T > 25^\circ\text{C}$  (67) and can thus be used to enhance the contrast. Changes in pH are, however, negligible, but competing guest molecules can alter the exchange dynamics of xenon into the cage (65).

The signal transfer is very efficient and can reveal target molecules even at fairly low concentrations. With molecular imaging, a high signal contrast of 50% was achieved with only  $\sim 1.3\text{-}\mu\text{M}$  concentration of NMR-active sensor and  $\sim 2.1\text{ }\mu\text{M}$  of dissolved, detectable xenon. Typical CEST experiments with signal changes of a few percent from thermally polarized protons require contrast agent concentrations of at least  $\sim 10\text{ }\mu\text{M}$  and are based on significantly higher concentrations of detectable nuclei (factor 2600 or 4400 for protons at 7 or 11 T, respectively, compared to xenon in Reference 41). The concentration of the detected target protein in the molecular imaging application was as low as 325 nM, and HYPER-CEST reduced acquisition time by 99.97% compared to conventional biosensor detection (41, 68).

For further optimization, the number of exchange sites can be significantly increased by dendrimeric amplification (69). Alternative detection techniques that are not based on the weak NMR signal of Faraday induction will also help to improve

---

**Low field:** magnetic field for encoding less than a few mT

---

sensitivity for biochemical/biomedical applications. For example, low-field detection (discussed in the following section) is a powerful tool in this context, especially because of the advantages of the xenon chemical shift range over the small-proton chemical shift range. Thus, only moderate prepolarization fields are required to encode molecular information in the xenon signal, and such techniques can be combined with optical magnetometer detection.

## 5. DETECTING NUCLEAR MAGNETIC RESONANCE IN LOW FIELD

As discussed above, NMR and MRI are usually carried out in a high magnetic field (>1 T). A strong magnetic field leads both to high polarization of the sample and to good detection sensitivity for conventional inductive coils. Furthermore, chemical shifts of most nuclei are only resolvable in a sufficiently strong magnetic field, as chemical shifts scale with field strength (5).

There are several limitations for high-field NMR/MRI, however. First, samples possessing large magnetic-susceptibility gradients disturb the field homogeneity, broadening spectral lines and distorting images (70). Examples include materials with metal components, such as metallic implants. Second, when the sample is enclosed by conductors, the small skin depth of the rf excitation pulses prohibit NMR measurements (71). For example, at a proton Larmor frequency of 100 MHz (2.4 T), the penetration depth of copper is only 10  $\mu\text{m}$ . A copper sheet thicker than 10  $\mu\text{m}$  will effectively prevent excitation of the nuclear spins and detection of the NMR signal.

In addition to these fundamental physical problems, there are also engineering and cost issues, such as:

1. The superconducting coils that generate the strong magnetic fields for high-field NMR and MRI are immobile, making measurements achievable only in a laboratory or hospital environment.
2. The availability of the cryogenics associated with superconducting magnets may also be an issue in many circumstances.
3. The bore of a high-field magnet is often not feasible for large objects.
4. The cost of the magnets and cryogenics is considerably high, limiting the use of high-field NMR/MRI to major facilities.

To overcome these limitations and therefore expand the applicability of NMR/MRI, researchers have extensively explored performing NMR/MRI at low fields (72–74). Here, we define low fields as magnetic fields lower than a few mT. (The Earth's magnetic field is  $\sim 0.05$  mT.) Intermediate-field NMR/MRI, also a booming research area, is not discussed in this review.

In general, low-field NMR/MRI can be divided into three stages: prepolarization, encoding, and detection. Because the nuclear polarization of the sample in a low field is insignificant, a prepolarization stage is usually required to provide sufficient initial polarization. Several methods are available for prepolarization, the most common of which involves strong ( $\sim 1$ -T) permanent magnets. High homogeneity of the magnetic field is not required in this case, as it is not used for spectral or spatial encoding.

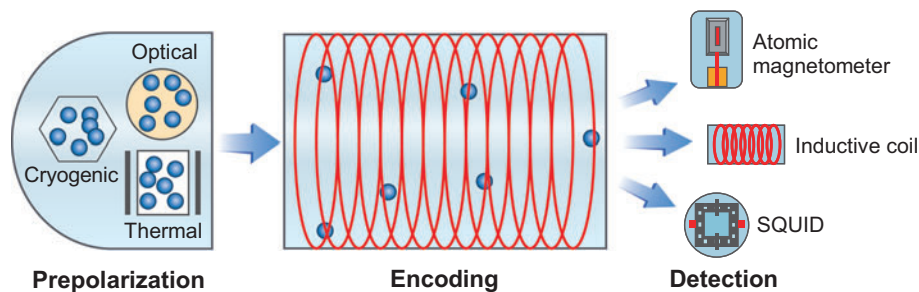


**Figure 8**

A schematic of low-field nuclear magnetic resonance/magnetic resonance imaging showing three stages: prepolarization, encoding, and detection. Prepolarization methods include thermal polarization by a strong magnetic field, optical hyperpolarization for xenon or helium, and polarization transfer from para- $\text{H}_2$  (generated by cryogenic cooling), among others. Detection can be conducted with an inductive coil, a superconducting quantum interference device (SQUID), or an atomic magnetometer.

Furthermore, cryogenics are not needed. Other prepolarization methods include optical pumping processes, such as those that produce hyperpolarized  $^{129}\text{Xe}$  and  $^3\text{He}$  gases (11), polarization transfer from para- $\text{H}_2$  (75), and dynamic nuclear polarization (76).

The encoding process, which is conducted in a weak and homogeneous field, is analogous to high-field encoding except for two differences. One is the Larmor frequency, which is in audio frequency range. Because of this, the penetration of the excitation pulse and the signal through conductive materials is significantly improved. The other difference is that only very weak gradients are required ( $\sim 0.1$  mT/m) for imaging, as they are much easier to generate than strong gradients.

Detection can be achieved via several possible techniques: conventional inductive detection, detection with superconducting quantum interference devices (SQUIDs), and laser detection using optical atomic magnetometers. A schematic of low-field NMR/MRI is illustrated in **Figure 8**. In the following sections, we discuss and compare these three detection techniques.

### 5.1. Faraday Inductive Detection

Using an inductive coil for low-field NMR/MRI detection is conceptually straightforward. By eliminating the superconducting magnets and cryogenics, the spectrometers become portable and less expensive. Early work on inductive detection of low-field NMR was attempted by Packard & Varian (77). However, accurate measurements had not been achieved until recent work by Appelt and colleagues (78), who reported NMR spectra detected by a tuned resonant circuit in the Earth's field in a remote area. The detection coil was composed of thousands of turns for improved efficiency. Because of the excellent homogeneity of the Earth's field, a linewidth of several millihertz was obtained, compared to 0.1 Hz in modern high-field NMR spectrometers. Heteronuclear J-coupling for a range of compounds was resolved with extraordinary

---

**SQUID:** superconducting quantum interference device

---

precision, i.e.,  $\pm 5$  mHz, which is more than one order of magnitude better than analogous high-field measurements. The J-coupling values are thus capable of serving as key parameters to distinguish chemicals containing heteronuclei, as chemical shift information is not resolvable in such low fields.

Multidimensional NMR is a powerful tool for further clarification of chemical structures. Robinson et al. reported the first two-dimensional correlation spectroscopy spectra of 1,4-difluorobenzene and 2,2,2-trifluoroethanol in the Earth's field (79). Both proton and fluorine nuclei appeared in the spectra: Higher frequency resonances arose from the protons and lower ones from fluorine. The fact that both types of nuclei appeared in the same spectrum is a unique feature of low-field NMR; this occurs because their Larmor frequencies are only slightly different compared to the excitation pulse width and detection bandwidth. This technique thus allows measurements of the relative abundance of these different nuclei in one chemical by a single NMR spectrum. The diagonal peaks reveal molecular orbital connectedness and atomic proximity, providing decisive and unambiguous information for structural identification.

Conventional inductive detection is also used for low-field MRI. Mohorič et al. reported a nicely designed MRI system for the Earth's field (80). A reference signal from a separate spectrometer was used to monitor the fluctuation of the Earth's field, creating a stable rotating frame for the measured signal. Sensitivity was improved by a rational design of the receiving coil and an audio frequency shield which resulted in an image with the smallest voxel on the order of  $50 \text{ mm}^3$ . On the application front, Halse and colleagues showed MR images of a pepper in the Earth's field (81). Because the  $B_0$  is only  $\sim 0.05$  mT, the imaging gradient is on the order of  $\sim 0.1$  mT/m, which is 2–3 orders of magnitudes weaker than conventional MRI. Thus, no high-power gradient amplifiers are required, meaning that low-field MRI apparatus consume less power and are more portable. The exceptional size and excellent homogeneity of the Earth's field enable imaging of samples of very large sizes. Practical applications include plant analysis and food inspection.

The major drawback of inductive detection in low field is its limited sensitivity, which is proportional to the strength of the magnetic field  $B_0$ . In the examples mentioned above, milliliters of samples are usually required, making inductive detection in low field not feasible for analyzing trace amounts of chemicals. Trace chemical analysis is important for applications such as monitoring chemical reactions or biochemical processes occurring on lab-on-a-chip devices. In order for low-field NMR and MRI techniques to be applicable for efficient chemical analysis, alternative detection techniques need to be developed. For this purpose, among others, NMR detection using SQUIDs and atomic magnetometers has been explored.

## 5.2. Superconducting Quantum Interference Devices

SQUIDs are based on the voltage oscillation of a superconducting loop interrupted by Josephson junctions (82). This oscillation is a function of the magnetic flux through the loop. Therefore, a SQUID acts as a flux-to-voltage transformer. Unlike a conventional inductive coil, SQUID can detect magnetic signal in an arbitrarily low

magnetic field without losing sensitivity; in other words, the sensitivity is independent of the magnetic field strength. The current state-of-the-art SQUID has reached sensitivities below  $1 \text{ fT}/(\text{Hz})^{1/2}$  for ac signal (83), sufficient for NMR measurements.

Initially, SQUID was used for detecting NMR signals of samples at liquid helium temperature, which was of limited practical potential. In the last decade, researchers have significantly expanded the applications of SQUID in NMR/MRI measurements for samples at room temperature. For example, McDermott et al. showed a SQUID-detected NMR spectrum of trimethyl phosphate (84). A linewidth of  $\sim 1 \text{ Hz}$  is obtained in a  $1.8\text{-}\mu\text{T}$   $B_0$  without shimming. The signature J-coupling between phosphorus and protons in trimethyl phosphate is obtained.

To demonstrate the advantage of low-field MRI in imaging objects with large magnetic-susceptibility gradients and objects enclosed in metal, Mößle and colleagues reported SQUID-detected MR images of a grid with a titanium bar and images of a pepper enclosed in an aluminum can, and compared them with corresponding high-field results (85). The first set of images revealed that the susceptibility distortion to the images due to the titanium bar was not pronounced in low field, in contrast to the images taken in high field. The images of the canned pepper showed no shielding factor of the metal for audio frequency excitation and signal, whereas images of the pepper were not obtainable in high field because of the effective shielding by the aluminum can.

Recent technical advances enable SQUID to be implemented for in vivo MRI. Mößle and coworkers employed a second-order SQUID gradiometer to obtain images of human forearm in  $\sim 100 \mu\text{T}$  (86). The subject was surrounded by a 3-mm-thin aluminum sheet to eliminate environmental noise. A 100-mT magnetic field was used for prepolarization. The resulting images clearly showed different tissues, with three-dimensional spatial resolution of  $2 \times 2 \times 8 \text{ mm}^3$ . Thus, SQUID MRI in low field offers a viable alternative for medical diagnosis.

One unique characteristic of MRI is its capacity to distinguish between different sections of the imaging object via contrast. In low field, contrast based on  $T_1$  relaxation is greatly enhanced (87). SQUID detection of low-field MRI is well-suited to realize this advantage because of its high sensitivity. Lee et al. (88) were able to demonstrate the outstanding  $T_1$  contrast of agarose solution (compared to solution without agarose) with a concentration as low as 0.25% at 0.01 mT, whereas no observable contrast was seen at 300 mT. Even though inductive detection is also applicable to measuring the enhanced low-field  $T_1$  contrast via field cycling, direct detection with SQUID drastically simplifies the measuring procedure and reduces the requirement of field homogeneity.

The ultrahigh sensitivity and maturity with regard to engineering make SQUID the current state-of-the-art technique for low-field NMR/MRI detection. It is applicable to numerous fields, ranging from chemical analysis to medical imaging. Like any other technique, however, SQUID also has several drawbacks. One is that the cryogenics needed for the superconducting loop impose constraints for the portability and feasibility of this technique. In addition, the electronic components, which improve sensitivity and detection efficiency, become very complicated for arrayed SQUIDs. These issues will likely be addressed in the next generation of SQUIDs.

### 5.3. Optical Atomic Magnetometer

Another high-sensitivity magnetometer is the optical atomic magnetometer, which has long been used for precise measurement of magnetic fields and fundamental physics parameters (89, 90). An atomic magnetometer utilizes the magneto-optical interactions between a laser beam and an alkali vapor. First, the incident laser beam, which has a near-resonance frequency to one of the electronic transitions of the alkali, generates a coherent ground state in the alkali vapor enclosed in a glass cell. The coherent alkali atoms interact with the probe beam (which can come from the same laser for pumping), resulting in an optical rotation of the polarization of the laser, or a dispersive absorption spectrum. The magneto-optical effects depend on the external magnetic field from the sample to be measured. Therefore, detection of the magnetic field is dependent upon the detection of photons, which can be measured with very high sensitivity.

For a given alkali element, the sensitivity of atomic magnetometers depends on the coherence time of the ground electronic state and the vapor density of the alkali (91). Two means of optimizing the sensitivity have been demonstrated. The Budker group used paraffin-coated alkali cells to minimize spin-destructive wall collisions and improve the coherence time of the ground state. The vapor cell was filled with pure vapor of an alkali metal, so the atomic density was in the high-vacuum regime. The ground-state coherence was preserved during thousands of collisions between the alkali atoms and the cell wall and lasted for seconds. The sensitivity of the magnetometer was thereby significantly improved. In this method, a single laser beam is often used for both pumping and probing, as the low-density alkali vapor only requires a low-power laser. A near-dc sensitivity of  $\sim 50$  fT/(Hz)<sup>1/2</sup> has been achieved with a 1-cm<sup>3</sup> <sup>87</sup>Rb cell (92). For ac signal detection, the sensitivity is several fT/(Hz)<sup>1/2</sup> (93).

The other approach, developed by Romalis and colleagues, uses buffer gases to eliminate the coherence-destroying collisions (94). The alkali atoms reach a spin-exchange relaxation-free regime in near-zero magnetic fields. Here the atomic density is much higher than that of the other approach. Two laser beams are usually used, one with relatively high power for pumping the high-density alkali vapor, one with low power for detection. Recently, Savukov et al. demonstrated that subfemtotesla sensitivity at  $\sim 20$  Hz can be achieved (95), a rate comparable to that of a SQUID magnetometer.

Application of atomic magnetometers in NMR was initially demonstrated by Yashchuk et al. (96), who measured the longitudinal magnetization of hyperpolarized xenon and obtained the  $T_1$  relaxation time of 14 min. Shortly after, a proton NMR spectrum at 20 Hz was obtained by Savukov et al. in  $\sim 0.5$   $\mu$ T (97). These pioneering works demonstrated that atomic magnetometry would become an alternative technique for the detection of faint NMR signals.

Since those experiments, other groups have employed novel NMR and MRI techniques with atomic magnetometry. Coupled with remote detection (described above), atomic magnetometers have been used in obtaining both NMR spectra and images. In a study of flow, Xu et al. (98) first demonstrated MR images detected by an atomic magnetometer with 1.6-mm spatial resolution and 0.1-s temporal resolution (**Figure 9**).

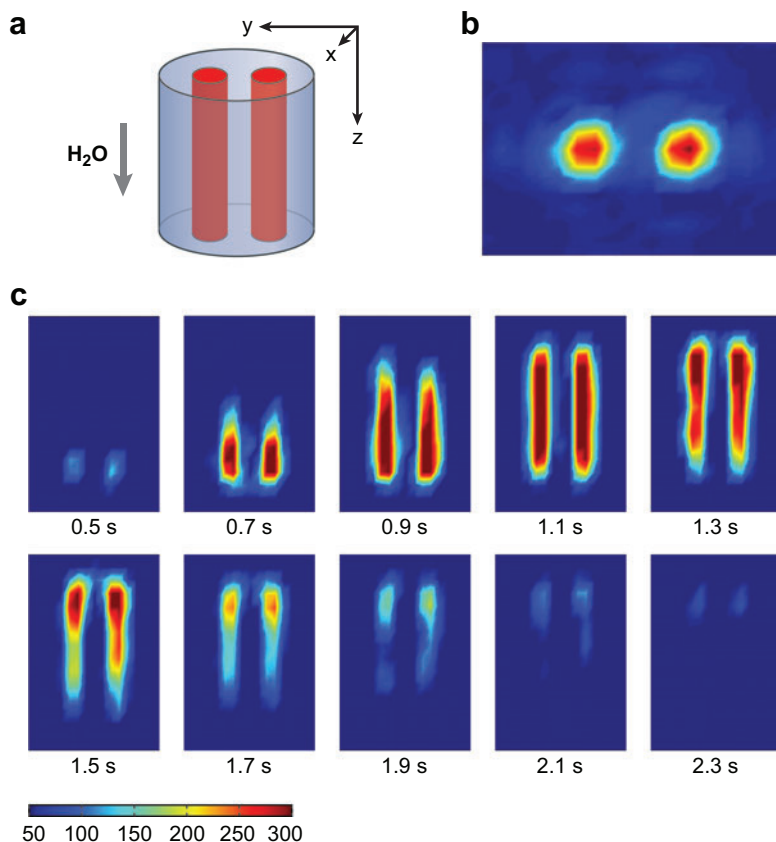


**Figure 9**

Magnetic resonance images detected with an atomic magnetometer. (a) The encoding volume. The two channels are 3.2 mm in diameter and 25 mm long, with a center-to-center spacing of 5.1 mm. (b) Image of the cross section perpendicular to the flow ( $xy$  plane) at  $t = 1.1$  s. (c) Time-resolved images in the  $yz$  plane. Measurements were obtained with a temporal interval of 0.1 s. Reproduced with permission from Reference 98. Copyright PNAS.

The spatial resolution is considerably better than that by inductive detection at low fields. It demonstrated the capability of atomic magnetometry as a viable and inexpensive alternative to high-field MRI. Extensive applications of this detection scheme can be expected, such as slow dynamics in microchannels or porous materials. Recent developments have shown that submillimeter resolution is also achievable in the Earth's field (S. Xu, et al., unpublished data).

For the in situ detection of NMR and MRI, atomic magnetometers need to be operated in rf mode to measure the Larmor precession of the nuclei. Romalis and colleagues pioneered rf atomic magnetometers and reported a sensitivity of  $\sim 1$  fT/Hz in a frequency range up to 99 kHz (99). A static water sample was prepolarized in situ and NMR spectra were obtained directly (100). The Romalis group offered a detailed discussion on implementing atomic magnetometry for NMR detection. Based on their simplified model, they concluded that atomic magnetometers have the advantage in sensitivity over inductive coils when  $B_0$  is less than  $\sim 1$  T.

A major motivation for developing alternative NMR/MRI detection techniques involves searching for a miniaturizable method for monitoring biological processes and chemical reactions on lab-on-a-chip devices. Atomic magnetometry has been

shown to possess such characteristics. Schwindt et al. used a magnetometer, with a total height of less than 3 mm, with an outstanding sensitivity of 5 pT (101). Because the distance of this detector to the sample is greatly reduced, the overall detection limit is improved. Applications in microanalysis are currently under way.

#### 5.4. Perspectives for Low-Field Magnetic Resonance

Among the three detection devices described above, SQUIDs and atomic magnetometers offer much better sensitivity than inductive coils in low fields. These devices, therefore, have greater potential in low-field NMR and MRI. Developments in SQUID techniques have advanced much further than have those in atomic magnetometry. Not surprisingly, the applications of SQUID in this field far surpass those of atomic magnetometers. However, compared to SQUID modality, atomic magnetometry requires no cryogenics, a significant advantage in both cost and portability. In terms of electronics, atomic magnetometers require much less complicated instrumentation as the signal is measured via photon detection, which allows for easier multichannel detection and miniaturization.

In addition to the techniques mentioned herein, other novel tools have been investigated for NMR detection without superconducting magnets. Rugar et al. (102) developed magnetic resonance force microscopy that is capable of measuring a single electron spin. Direct magneto-optical interaction between polarized nuclei and a laser beam has also been studied (103). All such innovative work will lead to more possibilities for low-field NMR and MRI.

##### SUMMARY POINTS

1. Remote detection NMR and MRI allows significant signal amplification for low-porosity systems due to the optimal filling factor of the detector.
2. TOF information allows material heterogeneities to be elucidated, making TOF an ideal tool for studying porous systems and microfluidic devices.
3. Chemical exchange of saturated spin systems represents an in situ version of remote detection with significant signal amplification.
4. Hyperpolarized, exchangeable xenon can be functionalized to encode specific molecular information and is an ideal candidate for saturation transfer experiments with further sensitivity enhancement in molecular imaging.
5. SQUIDs and atomic magnetometers are viable for alternative detection of low-field NMR and MRI.

##### FUTURE ISSUES

1. Remote detection will be applied for in vivo applications utilizing the natural blood flow of the body's circulatory system.

2. High-throughput chemical analysis and imaging for use with lab-on-a-chip devices will be necessary.
3. Which of the many exogenous CEST agents will be suitable for in vivo applications?
4. Will optimized CEST agents be able to compete with radionuclide tracers?
5. HYPER-CEST sensors for cell tracking will be demonstrated.
6. Complex pulse sequences in SQUID-detected and laser-detected NMR and MRI will be implemented.
7. SQUIDs and atomic magnetometers will be miniaturized.

## DISCLOSURE STATEMENT

The authors are not aware of any biases that might be perceived as affecting the objectivity of this review.

## ACKNOWLEDGMENTS

We remain, as always, grateful to Alex Pines for his guidance, advice, and support which reflect decades of innovation and the impact of magnetic resonance in chemistry. Much of the data presented here is representative of the work of many of the so-called Pinenuts collected over the past few years. We are grateful for all their countless hours of hard work, which has led to these exciting developments in magnetic resonance.

This work is supported by the Director, Office of Science, Office of Basic Energy Sciences and the Materials Sciences Division of the U.S. Department of Energy under contract DE-AC03-76SF0098. E.H. is supported by a fellowship from the U.S. Department of Homeland Security under DOE contract number DE-AC05-00OR22750. L.S. is supported by the Deutsche Forschungsgemeinschaft (SCHR 995/1-1) through an Emmy Noether Fellowship.

## LITERATURE CITED

1. Breitmaier E. 1993. *Structure Elucidation by NMR in Organic Chemistry*. New York: Wiley
2. Wüthrich K. 1986. *NMR of Proteins and Nucleic Acids*. New York: Wiley
3. Edelman R, Hesselink J, Zlatkin M. 1996. *Clinical Magnetic Resonance Imaging*. Philadelphia: Saunders
4. Callaghan PT. 1991. *Principles of Nuclear Magnetic Resonance Microscopy*. Oxford: Oxford Univ. Press
5. Abragham A. 1961. *Principles of Nuclear Magnetism*. Oxford: Oxford Univ. Press
6. Farrar TC, Becker ED. 1971. *Pulse and Fourier Transform NMR*. New York: Academic

7. Hoult DI, Richards RE. 1976. The signal-to-noise ratio of the nuclear magnetic resonance experiment. *J. Magn. Reson.* 24:71–85
8. Moule AJ, Spence MM, Han SI, Seeley JA, Pierce KL, et al. 2003. Amplification of xenon NMR and MRI by remote detection. *Proc. Natl. Acad. Sci. USA* 100:9122–27
9. Seeley JA, Han SI, Pines A. 2004. Remotely detected high-field MRI of porous samples. *J. Magn. Reson.* 167:282–90
10. Granwehr J, Harel E, Han SI, Garcia S, Pines A, et al. 2005. Time-of-flight flow imaging using NMR remote detection. *Phys. Rev. Lett.* 95:075503
11. Walker TG, Happer W. 1997. Spin-exchange optical pumping of noble gas nuclei. *Rev. Mod. Phys.* 69:629
12. Goodson BM. 2002. Nuclear magnetic resonance of laser-polarized noble gases in molecules, materials, and organisms. *J. Magn. Reson.* 155:157–216
13. Cohen MH, Mendelson KS. 1982. Nuclear magnetic resonance and the internal geometry of sedimentary rocks. *J. Appl. Phys.* 53:1127–35
14. Mansfield P, Turner R, Stehling MK. 1991. Echo-planar imaging: magnetic resonance imaging in a fraction of a second. *Science* 254:43–50
15. Gregory DM, Gerald RE, Botto RE. 1998. Pore-structure determinations of silica aerogels by  $^{129}\text{Xe}$  NMR spectroscopy and imaging. *J. Magn. Reson.* 131:327–35
16. Terskikh VV, Moudrakovski IL, Mastikhin VM. 1993.  $^{129}\text{Xe}$  nuclear magnetic resonance studies of the porous structure of silica gels. *J. Chem. Soc. Faraday Trans.* 89:4239–43
17. Terskikh VV, Moudrakovski IL, Breeze SR, Lang S, Ratcliffe CI, et al. 2002. A general correlation for the  $^{129}\text{Xe}$  NMR chemical shift-pore size relationship in porous silica-based materials. *Langmuir* 18:5653–56
18. Harel E, Granwehr J, Seeley JA. 2006. Multiphase imaging of gas flow in a nanoporous material using remote-detection NMR. *Nat. Mater.* 5:321–27
19. Taylor G. 1953. Dispersion of soluble matter in solvent flowing slowly through a tube. *Proc. R. Soc. London Ser. A* 219:186–203
20. Reichenauer G, Stumpf C, Fricke J. 1995. Characterization of  $\text{SiO}_2$ , rf and carbon aerogels by dynamic gas expansion. *J. Non-Cryst. Solids* 186:334–41
21. Emmerling A, Fricke J. 1992. Small angle scattering and the structure of aerogels. *J. Non-Cryst. Solids* 145:113–20
22. Schaefer DW, Keefer KD. 1986. Structure of random porous materials: silica aerogel. *Phys. Rev. Lett.* 56:2199–202
23. Bonardet JL, Fraissard J, Gédéon A, Springuel-Huet MA. 1999. Nuclear magnetic resonance of physisorbed  $\text{Xe-}^{129}$  used as a probe to investigate porous solids. *Catal. Rev.-Sci. Eng.* 41:115–225
24. Hilty C, McDonnell EE, Granwehr J, Pierce KL, Han SI, Pines A. 2005. Microfluidic gas-flow profiling using remote-detection NMR. *Proc. Natl. Acad. Sci. USA* 102:14960–63
25. Stone HA, Stroock AD, Ajdari A. 2004. Engineering flows in small devices: microfluidics toward a lab-on-a-chip. *Annu. Rev. Fluid Mech.* 36:381–411
26. Koop MU, de Mello AJ, Manz A. 1998. Chemical amplifications: continuous-flow PCR on a chip. *Science* 280:1046–48

27. Figeys D, Pinto D. 2001. Proteomics on a chip: promising developments. *Electrophoresis* 22:208–16
28. Haswell SJ, Middleton RJ, O’Sullivan B, Skelton V, Watts P, Styring P. 2001. The application of micro reactors to synthetic chemistry. *Chem. Commun.* 2001:391–98
29. Hong JW, Studer V, Hang G, Anderson WF, Quake SR. 2004. A nanoliter-scale nucleic acid processor with parallel architecture. *Nat. Biotechnol.* 22:435–39
30. Stroock AD, Dertinger SK, Ajdari A, Mezic I, Stone HA, Whitesides GM. 2002. Chaotic mixer for microchannels. *Science* 295:647–51
31. Cristobal G, Arbouet L, Sarrazin F, Talaga D, Bruneel J-L, et al. 2006. On-line laser Raman spectroscopic probing of droplets engineered in microfluidic devices. *Lab Chip* 6:1140–46
32. Zhu L, Lee CS, DeVoe DL. 2006. Integrated microfluidic UV absorbance detector with attomol-level sensitivity for BSA. *Lab Chip* 6:115–20
33. Wensink H, Benito-Lopez F, Hermes DC, Verboom W, Gardeniers HJGE, et al. 2005. Measuring reaction kinetics in a lab-on-a chip by microcoil NMR. *Lab Chip* 5:280–84
34. Harel E, Hilty C, Koen K, McDonnell EE, Pines A. 2007. Time-of-flight flow imaging of two-component flow inside a microfluidic chip. *Phys. Rev. Lett.* 98:017601
35. Ehrmann K, Gersbach M, Pascoal P, Vincent F, Massin C, et al. 2006. Sample patterning on NMR surface microcoils. *J. Magn. Reson.* 178:96–105
36. Sakellariou D, Le Goff G, Jacquinet J-F. 2007. High-resolution, high-sensitivity NMR of nanolitre anisotropic samples by coil spinning. *Nature* 447:694–97
37. Olson DL, Peck TL, Webb AG, Magin RL, Sweedler JV. 1995. High-resolution microcoil <sup>1</sup>H-NMR for mass-limited, nanoliter-volume samples. *Science* 270:1967–70
38. Bouchard LS, Budker D, Harel E, Ledbetter M, Lowery T, et al. 2007. U.S. patent pending
39. Massoud TF, Gambhir SS. 2003. Molecular imaging in living subjects: seeing fundamental biological processes in a new light. *Genes Dev.* 17:545–80
40. Ward KM, Aletras AH, Balaban RS. 2000. A new class of contrast agents for MRI based on proton chemical exchange dependent saturation transfer (CEST). *J. Magn. Res.* 143:79–87
41. Schröder L, Lowery TJ, Hilty C, Wemmer DE, Pines A. 2006. Molecular imaging using a targeted magnetic resonance hyperpolarized biosensor. *Science* 314:432–33
42. Forsén S, Hoffman R. 1963. Study of moderately rapid chemical exchange reactions by means of nuclear magnetic double resonance. *J. Chem. Phys.* 39(11):2892–901
43. McConnell HM. 1958. Reaction rates by nuclear magnetic resonance. *J. Chem. Phys.* 28:430–31
44. Bryant RG. 1996. The dynamics of water-protein interactions. *Annu. Rev. Biophys. Biomol. Struct.* 25:29–53

45. Zhou J, Wilson DA, Zhe Sun P, Klaus JA, van Zijl PCM. 2004. Quantitative description of proton exchange processes between water and endogenous and exogenous agents for WEX, CEST, and APT experiments. *Magn. Reson. Med.* 51:945–52
46. Zhou J, Payen J-F, Wilson DA, Traystman RJ, van Zijl PCM. 2003. Using the amide proton signals of intracellular proteins and peptides to detect pH effects in MRI. *Nat. Med.* 9:1085–90
47. van Zijl PCM, Zhou J, Mori N, Payen J-F, Wilson D, Mori S. 2003. Mechanism of magnetization transfer during on-resonance water saturation: a new approach to detect mobile proteins, peptides, and lipids. *Magn. Reson. Med.* 49:440–49
48. Zhou J, van Zijl PCM. 2006. Chemical exchange saturation transfer imaging and spectroscopy. *Progr. NMR Spectrosc.* 48:109–36
49. Ward KM, Balaban RS. 2000. Determination of pH using water protons and chemical exchange dependent saturation transfer (CEST). *Magn. Reson. Med.* 44:799–802
50. Goffeney N, Bulte JW, Duyn J, Bryant LH Jr, van Zijl PC. 2001. Sensitive NMR detection of cationic-polymer-based gene delivery systems using saturation transfer via proton exchange. *J. Am. Chem. Soc.* 123:8628–29
51. Snoussi K, Bulte JW, Guéron M, van Zijl PCM. 2003. Sensitive CEST agents based on nucleic acid imino proton exchange: detection of poly(rU) and of a dendrimer-poly(rU) model for nucleic acid delivery and pharmacology. *Magn. Reson. Med.* 49:998–1005
52. Zhou J, Lal B, Wilson DA, Larterra J, van Zijl PCM. 2003. Amide proton transfer (APT) contrast for imaging of brain tumors. *Magn. Reson. Med.* 50:1120–26
53. McMahon MT, Gilad AA, Zhou J, Sun PZ, Bulte JW, van Zijl PC. 2006. Quantifying exchange rates in chemical exchange saturation transfer agents using the saturation time and saturation power dependencies of the magnetization transfer effect on the magnetic resonance imaging signal (QUEST and QUESP): Ph calibration for poly-L-lysine and a starburst dendrimer. *Magn. Reson. Med.* 55:836–47
54. Sun PZ, van Zijl PCM, Zhou J. 2005. Optimization of the irradiation power in chemical exchange dependent saturation transfer experiments. *J. Magn. Reson.* 175:193–200
55. Zhang S, Winter P, Wu K, Sherry DK. 2001. A novel europium(III)-based MRI contrast agent. *J. Am. Chem. Soc.* 123:1517–18
56. Aime S, Carrera C, Delli Castelli D, Geniatti Crich S, Terreno E. 2005. Tunable imaging of cells labeled with MRI-PARACEST agents. *Angew. Chem. Int. Ed.* 44:1813–15
57. Zhang S, Merritt M, Woessner DE, Lenkinski RE, Sherry DA. 2003. PARACEST agents: modulating MRI contrast via water proton exchange. *Acc. Chem. Res.* 36:783–90
58. Woods M, Woessner DE, Sherry DA. 2006. Paramagnetic lanthanide complexes as PARACEST agents for medical imaging. *Chem. Soc. Rev.* 35:500–11
59. Aime S, Delli Castelli D, Terreno E. 2002. Novel pH-reporter MRI contrast agents. *Angew. Chem. Int. Ed.* 41(22):4334–36

60. Terreno E, Delli Castelli D, Cravotto G, Milone L, Aime S. 2004. Ln(III)-DOTAMGly complexes: a versatile series to assess the determinants of the efficacy of paramagnetic chemical exchange saturation transfer agents for magnetic resonance imaging applications. *Invest. Radiol.* 39:235–43
61. Spence MM, Ruiz EJ, Rubin SM, Lowery TJ, Winssinger N, et al. 2004. Development of a functionalized xenon biosensor. *J. Am. Chem. Soc.* 126:15287–94
62. Garcia S, Chavez L, Lowery TJ, Han S-I, Wemmer DE, Pines A. 2007. Sensitivity enhancement by exchange mediated magnetization transfer of the xenon biosensor signal. *J. Magn. Reson.* 184(1):72–77
63. Goodson BM. 1999. Using injectable carriers of laser-polarized noble gases for enhancing NMR and MRI. *Concepts Magn. Reson.* 11(4):203–23
64. Lowery TJ, Rubin SM, Ruiz EJ, Spence MM, Winssinger N, et al. 2003. Applications of laser-polarized  $^{129}\text{Xe}$  to biomolecular assays. *Magn. Reson. Imag.* 21(10):1235–39
65. Bartik K, Luhmer L, Dutasta J-P, Collet A, Reisse J. 1998.  $^{129}\text{Xe}$  and  $^1\text{H}$  NMR study of the reversible trapping of xenon by cryptophane-A in organic solution. *J. Am. Chem. Soc.* 120(4):784–91
66. Spence MM, Rubin SM, Dimitrov IE, Ruiz EJ, Wemmer DE, et al. 2001. Functionalized xenon as a biosensor. *Proc. Natl. Acad. Sci. USA* 98:10654–57
67. Lowery TJ, Garcia S, Chavez L, Ruiz EJ, Wu T, et al. 2006. Optimization of xenon biosensors for detection of protein interactions. *ChemBioChem* 7:65–73
68. Hilty C, Lowery TJ, Wemmer DE, Pines A. 2006. Spectrally resolved magnetic resonance imaging of a xenon biosensor. *Angew. Chem. Int. Ed.* 45(1):70–73
69. Mynar JL, Lowery TJ, Wemmer DE, Pines A, Frechet JM. 2006. Xenon biosensor amplification via dendrimer-cage supramolecular constructs. *J. Am. Chem. Soc.* 128(19):6334–35
70. Ludecke KM, Roschmann P, Tischler R. 1993. Susceptibility artefacts in NMR imaging. *Magn. Reson. Imaging* 3:329–43
71. Bennett CR, Wang PS, Donahue MJ. 1996. Artifacts in magnetic resonance imaging from metals. *J. Appl. Physiol.* 79:4712–14
72. Béné GJ. 1980. Nuclear magnetism of liquid system in the Earth field range. *Phys. Rep.* 58:213–67
73. Stepišnik J, Kos M, Planinšič G, Eržen V. 1994. Strong non-uniform magnetic field for self-diffusion measurement by NMR in the earth's magnetic field. *J. Magn. Reson. A* 107:167–72
74. Appelt S, Häsing FW, Kühn H, Perlo J, Blümich B. 2005. Mobile high resolution xenon nuclear magnetic resonance spectroscopy in the earth's magnetic field. *Phys. Rev. Lett.* 94:197602
75. Bowers CR, Weitekamp DP. 1986. Transformation of symmetrization order to nuclear-spin magnetization by chemical reaction and nuclear magnetic resonance. *Phys. Rev. Lett.* 57:2645–48
76. Slichter CP. 1990. *Principles of Nuclear Magnetic Resonance*. New York: Springer-Verlag
77. Packard M, Varian R. 1954. Free nuclear induction in the Earth's magnetic field. *Phys. Rev.* 93:941

78. Appelt S, Kühn H, Häsing FW, Blümich B. 2006. Chemical analysis by ultrahigh-resolution nuclear magnetic resonance in the Earth's magnetic field. *Nat. Phys.* 2:105–9
79. Robinson JN, Coy A, Dykstra R, Eccles CD, Hunter MW, et al. 2006. Two-dimensional NMR spectroscopy in Earth's magnetic field. *Magn. Reson.* 182:343–47
80. Mohorič A, Planinšič G, Kos M, Duh A, Stepišnik J. 2004. Magnetic resonance imaging system based on Earth's magnetic field. *Instrum. Sci. Technol.* 32:655–67
81. Halse ME, Coy A, Dykstra R, Eccles C, Hunter M, et al. 2006. A practical and flexible implementation of 3D MRI in the Earth's magnetic field. *J. Magn. Reson.* 182:75–83
82. Clarke J. 1996. SQUID fundamentals. In *SQUID Sensors: Fundamentals, Fabrication, and Applications*, ed. H Weinstock, pp. 1–62. Dordrecht, Netherlands: Kluwer Acad.
83. Kleiner R, Koelle F, Ludwig F, Clarke J. 2004. Superconducting quantum interference devices: state of the art and applications. *Proc. IEEE* 92:1534–48
84. McDermott R, Trabesinger AH, Mück M, Hahn EL, Pines A, et al. 2002. Liquid-state NMR and scalar couplings in microtesla magnetic fields. *Science* 295:2247–49
85. Mößle M, Han S-I, Myers WR, Lee S-K, Kelso N, et al. 2006. SQUID-detected microtesla MRI in the presence of metal. *J. Magn. Reson.* 179:146–51
86. Mößle M, Myers WR, Lee S-K, Kelso N, Hatridge M, et al. 2005. SQUID-detected in vivo MRI at microtesla magnetic fields. *IEEE Trans. Appl. Supercond.* 15:757–60
87. Macovski A, Conolly S. 1993. Novel approaches to low-cost MRI. *Magn. Reson. Med.* 30:221–30
88. Lee SK, Mößle M, Myers WR, Kelso N, Trabesinger AH, et al. 2005. SQUID-detected MRI at 132 microT with T1-weighted contrast established at 10 microT–300 mT. *Magn. Reson. Med.* 53:9–14
89. Dehmelt HG. 1957. Modulation of a light beam by precessing absorbing atoms. *Phys. Rev.* 105:1924–25
90. Dupont-Roc J, Haroche S, Cohen-Tannoudji C. 1969. Detection of very weak magnetic fields (10–9 gauss) by Rb 87 zero-field level crossing resonances. *Phys. Lett. A* 28:638–39
91. Budker D, Romalis MV. 2007. Optical magnetometry. *Nat. Phys.* 3:227–34
92. Xu S, Rochester SM, Yashchuk VV, Donaldson MH, Budker D. 2006. Construction and applications of an atomic magnetic gradiometer based on nonlinear magneto-optical rotation. *Rev. Sci. Instrum.* 77:083106
93. Ledbetter MP, Acosta VM, Rochester SM, Budker D, Pustelny S, et al. 2007. Detection of radio-frequency magnetic fields using nonlinear magneto-optical rotation. *Phys. Rev. A* 75:023405
94. Allred JC, Lyman RN, Komack TW, Romalis MV. 2002. High-sensitivity atomic magnetometer unaffected by spin-exchange relaxation. *Phys. Rev. Lett.* 89:130801
95. Kominis IK, Kornack TW, Allred JC, Romalis MV. 2003. A subfemtotesla multichannel atomic magnetometer. *Nature* 422:596–99

96. Yashchuk VV, Granwehr J, Kimball DF, Rochester SM, Trabesinger AH, et al. 2004. Hyperpolarized xenon nuclear spins detected by optical atomic magnetometry. *Phys. Rev. Lett.* 93:160801
97. Savukov IM, Romalis MV. 2005. NMR detection with an atomic magnetometer. *Phys. Rev. Lett.* 94:123001
98. Xu S, Yashchuk VV, Donaldson MH, Rochester SM, Budker D, Pines A. 2006. Magnetic resonance imaging with an optical atomic magnetometer. *Proc. Natl. Acad. Sci. USA* 103:12668–71
99. Savukov IM, Seltzer SJ, Romalis MV, Sauer KL. 2005. Tunable atomic magnetometer for detection of radio-frequency magnetic fields. *Phys. Rev. Lett.* 95:063004
100. Savukov IM, Selter SJ, Romalis MV. 2007. Detection of NMR signals with a radio-frequency atomic magnetometer. *J. Magn. Reson.* 185:227–33
101. Schwindt PDD, Lindseth B, Knappe S, Shah V, Kitching J, et al. 2007. A chip-scale atomic magnetometer with improved sensitivity using the Mx technique. *Appl. Phys. Lett.* 90:081102
102. Rugar D, Budakian R, Mamin HJ, Chui BW. 2004. Single spin detection by magnetic resonance force microscopy. *Nature* 430:329–32
103. Savukov IM, Lee SK, Romalis MV. 2006. Optical detection of liquid-state NMR. *Nature* 442:1021–24



# Contents

A Personal Journey of Discovery: Developing Technology and Changing Biology <i>Lee Hood</i> .....	1
Spectroscopic and Statistical Techniques for Information Recovery in Metabonomics and Metabolomics <i>John C. Lindon and Jeremy K. Nicholson</i> .....	45
Mass Spectrometry for Rapid Characterization of Microorganisms <i>Plamen A. Demirev and Catherine Fenselau</i> .....	71
Scanning Electrochemical Microscopy <i>Shigeru Amemiya, Allen J. Bard, Fu-Ren F. Fan, Michael V. Mirkin, and Patrick R. Unwin</i> .....	95
Novel Detection Schemes of Nuclear Magnetic Resonance and Magnetic Resonance Imaging: Applications from Analytical Chemistry to Molecular Sensors <i>Elad Harel, Leif Schröder, and Shoujun Xu</i> .....	133
Chemical Cytometry: Fluorescence-Based Single-Cell Analysis <i>Daniella Cohen, Jane A. Dickerson, Colin D. Whitmore, Emily H. Turner, Monica M. Palcic, Ole Hindsgaul, and Norman J. Dovichi</i> .....	165
Chemical Analysis of Single Cells <i>Laura M. Borland, Sumith Kottegoda, K. Scott Phillips, and Nancy L. Allbritton</i> .....	191
Ion Chemistry in the Interstellar Medium <i>Theodore P. Snow and Veronica M. Bierbaum</i> .....	229
Plasma Diagnostics for Unraveling Process Chemistry <i>Joshua M. Stillabn, Kristina J. Trevino, and Ellen R. Fisher</i> .....	261
Biomolecule Analysis by Ion Mobility Spectrometry <i>Brian C. Bobrer, Samuel I. Merenbloom, Stormy L. Koeniger, Amy E. Hilderbrand, and David E. Clemmer</i> .....	293
In Vitro Electrochemistry of Biological Systems <i>Kelly L. Adams, Maja Puchades, and Andrew G. Ewing</i> .....	329

Current Applications of Liquid Chromatography/Mass Spectrometry in Pharmaceutical Discovery After a Decade of Innovation <i>Bradley L. Ackermann, Michael J. Berna, James A. Eckstein, Lee W. Ott, and Ajai K. Chaudhary</i> .....	357
Optical Probes for Molecular Processes in Live Cells <i>Yoshio Umezawa</i> .....	397
Cell Culture Models in Microfluidic Systems <i>Ivar Meyvantsson and David J. Beebe</i> .....	423
Peptides in the Brain: Mass Spectrometry–Based Measurement Approaches and Challenges <i>Lingjun Li and Jonathan V. Sweedler</i> .....	451
Analysis of Atmospheric Aerosols <i>Kimberly A. Prather, Courtney D. Hatch, and Vicki H. Grassian</i> .....	485
Multiplexed Spectroscopic Detections <i>Kyle D. Bake and David R. Walt</i> .....	515
Terrestrial Analysis of the Organic Component of Comet Dust <i>Scott A. Sandford</i> .....	549
High-Resolution Mass Spectrometers <i>Alan G. Marshall and Christopher L. Hendrickson</i> .....	579
Surface-Enhanced Raman Spectroscopy <i>Paul L. Stiles, Jon A. Dieringer, Nilam C. Shah, and Richard P. Van Duyne</i> .....	601
Time-Resolved Microdialysis for In Vivo Neurochemical Measurements and Other Applications <i>Kristin N. Schultz and Robert T. Kennedy</i> .....	627
Applications of Ultrafast Lasers for Optical Measurements in Combusting Flows <i>James R. Gord, Terrence R. Meyer, and Sukesh Roy</i> .....	663
Matrix-Assisted Laser Desorption/Ionization Imaging Mass Spectrometry for the Investigation of Proteins and Peptides <i>Kristin E. Burnum, Sara L. Frappier, and Richard M. Caprioli</i> .....	689
Formation and Characterization of Organic Monolayers on Semiconductor Surfaces <i>Robert J. Hamers</i> .....	707
Nanoscope Porous Sensors <i>John J. Kasianowicz, Joseph W.F. Robertson, Elaine R. Chan, Joseph E. Reiner, and Vincent M. Stanford</i> .....	737

Combining Self-Assembled Monolayers and Mass Spectrometry for Applications in Biochips <i>Zachary A. Gurard-Levin and Milan Mrksich</i> .....	767
Liposomes: Technologies and Analytical Applications <i>Aldo Jesorka and Owe Orwar</i> .....	801
Fundamentals of Protein Separations: 50 Years of Nanotechnology, and Growing <i>David A. Egas and Mary J. Wirth</i> .....	833
Functional and Spectroscopic Measurements with Scanning Tunneling Microscopy <i>Amanda M. Moore and Paul S. Weiss</i> .....	857
Coherent Anti-Stokes Raman Scattering Microscopy: Chemical Imaging for Biology and Medicine <i>Conor L. Evans and X. Sunney Xie</i> .....	883